

## Article

# An Analysis of Jet Noise Characteristics in the Compressible Turbulent Mixing Layer of a Standard Nozzle

Guozhen Mu <sup>1,\*</sup>, Qiongying Lyu <sup>1</sup> and Yiming Li <sup>2</sup>

<sup>1</sup> Jilin Province Innovation Center of Aerodynamic Science and Technology, Changchun University of Science and Technology, Changchun 130022, China

<sup>2</sup> School of Materials Science and Engineering, Taiyuan University of Technology, Taiyuan 030024, China

\* Correspondence: muguozhen@mails.cust.edu.cn

**Abstract:** In this paper, we seek to understand the influence of TPS standard nozzle shape on jet noise and improve the accuracy of flow and pressure ratio of aeronautical simulation. Through the structural design of an equal-diameter nozzle and a standard nozzle, a concentric dichotomy monitoring point arrangement scheme is proposed for its flow field and sound field, and the free flow of the jet is used to realize  $k - \epsilon$ . The model is solved by hydrodynamics to analyze the flow characteristics of the turbulent boundary layer, and the near-field and far-field characteristics of jet noise are analyzed by using the Lighthill equation excited by a quadrupole under fluid input, revealing the turbulent velocity and turbulent kinetic energy and other relevant fluid characteristics of the two nozzles under a single variable, and analyzing the near-field and far-field noise pressure levels and directivity of the two nozzles at a specific frequency. When the boundary conditions are consistent, the change trends and laws of the two kinds of nozzles in the turbulent jet flow field are almost the same, and the eddy viscosity extreme value of the standard nozzle is 0.02 higher than that of the equal-diameter nozzle, while the static temperature extreme value is 8 K, but they have a great impact in the noise field, mainly reflected in the noise decreasing law, noise directivity and low-frequency noise distribution. The mean value of noise extremes of standard nozzles at four frequencies is 2 dB higher than that of equal-diameter nozzles. The relative characteristics of the two nozzles can be used to design through the actual demand conditions of the flow field and the sound field by providing a reference for the customized parameter design of the standard nozzle.

**Keywords:** nozzle; concentric dichotomy; turbulent boundary layer; flow field analysis; noise characteristics



**Citation:** Mu, G.; Lyu, Q.; Li, Y. An Analysis of Jet Noise Characteristics in the Compressible Turbulent Mixing Layer of a Standard Nozzle. *Machines* **2022**, *10*, 826. <https://doi.org/10.3390/machines10100826>

Academic Editor: César M. A. Vasques

Received: 12 August 2022

Accepted: 13 September 2022

Published: 20 September 2022

**Publisher's Note:** MDPI stays neutral with regard to jurisdictional claims in published maps and institutional affiliations.



**Copyright:** © 2022 by the authors. Licensee MDPI, Basel, Switzerland. This article is an open access article distributed under the terms and conditions of the Creative Commons Attribution (CC BY) license (<https://creativecommons.org/licenses/by/4.0/>).

## 1. Introduction

Aerospace is a comprehensive entity attracting worldwide attention [1–3]. Taking into account the industry's consistent pursuit of low noise levels [4], with the rapid development of the aero-engine so that the aircraft can fly at a higher supersonic speed, the damage caused by airport noise pollution [5] and high-intensity sound pressure level to the environment and crew must be addressed [6]. A turbine power simulator [7] (TPS) is a scale model of an aero-engine, which has a replaceable nozzle and can simulate the intake and exhaust effects and noise response of the actual engine. The Lighthill theory [8] has found that the interaction of turbulence is a major cause of noise [9,10]. Therefore, the nozzle which produces turbulence in an aero-engine has a significant influence on the noise field. However, the randomness of turbulence therefore makes it difficult to study the relationship between nozzle shape and noise.

The jet noise experiment is a conventional research method, which includes an acoustic measurement of a supersonic axisymmetric jet [11,12], a sawtooth jet with noise reduction [13–15] and a multi stream axisymmetric jet [16–18]. In order to better study the characteristics of jet noise, numerical simulation [19–24] and experimental analysis are carried out to promote the development of jet noise [25]. James Bridges [26] showed the flow

field and far-field acoustic properties of various sawtooth nozzles to verify that velocity gradients are the key to noise generation. Jawahar HK [27] proved that the V-nozzle effectively reduces noise through wavelet decomposition. Proença [28] mainly dealt with the empirical formulas of turbulent characteristic scale and vortex convection velocity, C.E. Tinney [29] mainly studied the variation of the supersonic near pressure field, R.E.A. Arndt [30] mainly studied the inhomogeneity of the circular nozzle jet, and the sensor settings in the three papers all conformed to the traditional layout method.

Both civil aviation engines and military aviation engines have been studied with purpose of noise reduction, focusing on the impact of nozzle shape on flow field and noise, so as to promote the advantages of the next generation of aviation. It is difficult to promote the rapid development of jet noise with high full simulation experimental funds and complex logistical support. Scale experiments have become the mainstream of rapid mobile data system updating.

On the basis of previous research ideas, this paper proposes analyzing the jet noise characteristics of the standard nozzle of the turbine power simulator (TPS) by taking the equal-diameter nozzle as the control group, and proves the rationality of the layout of the new monitoring field. It is concluded that the nozzle shape of the turbine power simulator (TPS) has an impact on the turbulent core layer of the jet flow field when the compressed air pressure is 212,782 Pa and the compressed air temperature is 303 K. The noise decreasing law and directivity characteristics of the near and far fields of the noise field are revealed. The flow field and sound field characteristics of the two scale nozzles of TPS can provide the optimal direction for the parameter design of the TPS nozzle.

## 2. Sound Source Excitation and Microphone Array

This paper mainly studies the jet noise of the standard nozzle, which requires joint simulation of fluid dynamics and aeroacoustics and experimental verification. The monitoring point setting is particularly important. The research scheme design and monitoring point arrangement will be carried out below.

### 2.1. Conceptual Design

As special equipment of the turbine power simulator (TPS), the standard nozzle is hoisted in the nacelle to detect and calibrate the residual stress of the balance and air bridge system of the aircraft model. In order to discuss the influence of nozzle structure on jet noise, an equal-diameter nozzle is introduced. In order to conduct a single variable experiment, the cross-sectional area of the jet outlet is consistent with that of the standard nozzle, and the outlet flow satisfies the flow formula [31].

$$\dot{m}_{out} = K \frac{P^* A_{out}}{\sqrt{T^*}} q(Ma) \quad (1)$$

$$K = \sqrt{\frac{k}{R} \left( \frac{2}{k+1} \right)^{\frac{k+1}{k-1}}} \quad (2)$$

$$q(Ma) = Ma \left[ \frac{2}{k+1} \left( 1 + \frac{k-1}{2} Ma^2 \right) \right]^{-\frac{k+1}{2(k-1)}} \quad (3)$$

where  $\dot{m}_{out}$  is the mass flow of the nozzle jet,  $k$  is the adiabatic index of the air,  $P^*$  is the total pressure of the air,  $T^*$  is the total temperature of the air,  $A_{out}$  is the cross-sectional area of the nozzle jet outlet, and  $Ma$  is the Mach number. In the standard nozzle jet,  $k = 1.4$ ,  $R = 287.06 \text{ J}/(\text{kg} \cdot \text{K})$ . According to the flow formula, under a given  $Ma$ ,  $\dot{m}_{out} / A_{out}$  is directly proportional to the total pressure and inversely proportional to the square root of the total temperature. Therefore, the cross-sectional area of the equal-diameter nozzle and standard nozzle is consistent in this comparative experiment to examine the influence of nozzle structure on jet noise. Owing to the limitation of test conditions, the TPS Standard Nozzle scale model 1:15 was analyzed [32].

In Figure 1, (a) is the structure diagram of the equal-diameter nozzle, (b) is the structure diagram of the standard nozzle, (c) is the 3D-printed object, and the outlet diameter is  $y = 0.1$ ,  $a = 5.830904$ ,  $b = 0.1$ , and  $X_{\max} = 0.35$ .

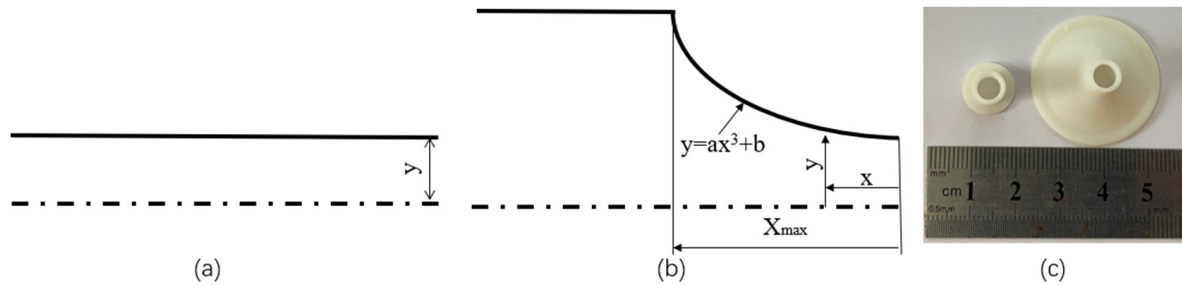


**Figure 1.** Structural schematic and physical diagram of the equal-diameter nozzle and standard nozzle.

### 2.2. Layout of Near-Field Monitoring Points

In order to better understand the near-field characteristics of the jet noise of the compressible mixing layer of the standard nozzle jet, a near-field solution rectangular area with a length of 500 mm and a width of 50 mm is arranged with the jet center as the origin, and nine monitoring points and three detection lines are arranged according to the dichotomy method to analyze the characteristics of the jet flow field and sound field, as shown in the figure.

In Figure 2, detection line 01–03 is obtained by the deflection of the jet axis 01–05 by  $5.484^\circ$ , detection line 01–04 is obtained by the deflection of the jet axis 01–05 by  $2.748^\circ$ , and detection line 01–15 is obtained by the deflection of the jet axis 01–05 by  $1.375^\circ$ .

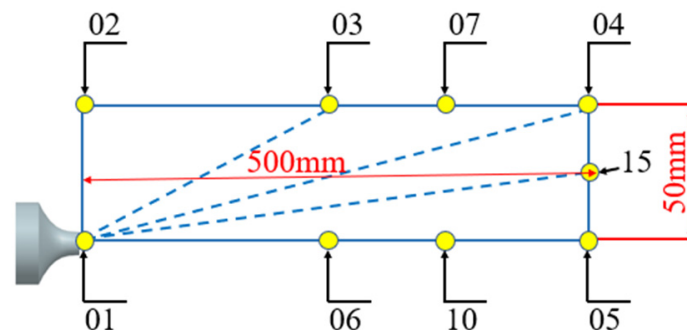


**Figure 2.** Layout of near-field monitoring points of the equal-diameter nozzle and standard nozzle.

### 2.3. Arrangement of Far-Field Monitoring Points

The far-field noise field of standard nozzle jet compressible mixed-layer jet is based on the jet center as the origin, and a far-field solution rectangular area with a length of 2000 mm and a width of 1000 mm is arranged, and a concentric bisection method is proposed to arrange 15 monitoring points and 3 detection lines to analyze the jet flow field and sound field characteristics, as shown in the figure. The reference line where the 24 detection points are located is an arc with a radius of 1000 mm, and the reference line where the 30 monitoring points are located is an arc with a radius of 1500 mm.

In Figure 3, the detection line 01–03 is obtained by the deflection of the jet axis 01–45 by  $26.565^\circ$ , the detection line 01–43 is obtained by the deflection of the jet axis 01–18 by  $14.036^\circ$ , and the detection line 01–44 is obtained by the deflection of the jet axis 01–18 by  $7.125^\circ$ .

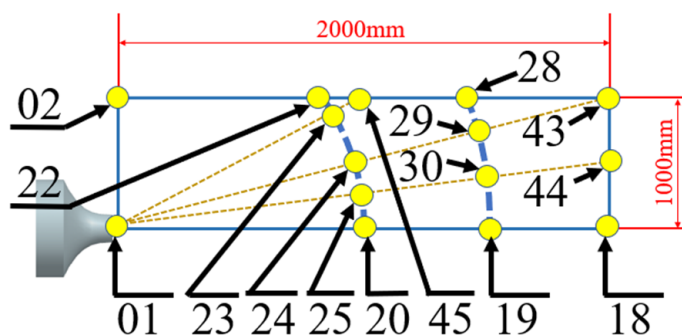


Figure 3. Schematic diagram for the arrangement of remote field monitoring points of the equal-diameter nozzle and standard nozzle.

### 3. Study on Correlation of Flow Field

The analysis of jet noise is inextricably linked to the numerical simulation of the jet flow field. The fluid in this paper is consistent and compressible, and the governing equations and turbulent models are unsteady and compressible. The jet satisfies the Realizable  $k - \epsilon$  model of jet free flow, and the transport equations for  $k$  and  $\epsilon$  are as follows [7].

$$\frac{\partial(\rho k)}{\partial t} + \frac{\partial(\rho k u_i)}{\partial x_i} = \frac{\partial}{\partial x_j} \left[ \left( \mu + \frac{\mu_i}{\sigma_k} \right) \frac{\partial k}{\partial x_j} \right] + G_k - \rho \epsilon \tag{4}$$

$$\frac{\partial(\rho \epsilon)}{\partial t} + \frac{\partial(\rho \epsilon u_i)}{\partial x_i} = \frac{\partial}{\partial x_j} \left[ \left( \mu + \frac{\mu_i}{\sigma_\epsilon} \right) \frac{\partial \epsilon}{\partial x_j} \right] + \rho C_1 E \epsilon - \rho C_2 \frac{\epsilon^2}{k + \sqrt{v \epsilon}} \tag{5}$$

Empirical constant:

$$\sigma_k = 1.0 \tag{6}$$

$$\sigma_\epsilon = 1.2 \tag{7}$$

Coefficient:

$$C_2 = 1.9 \tag{8}$$

$$C_1 = \max \left( 0.43, \frac{\eta}{\eta + 5} \right) \tag{9}$$

$$\eta = (2E_{ij} \cdot E_{ij})^{1/2} \frac{k}{\epsilon} \tag{10}$$

Time average strain rate:

$$E_{ij} = \frac{1}{2} \left( \frac{\partial u_i}{\partial x_j} + \frac{\partial u_j}{\partial x_i} \right) \tag{11}$$

$$\mu_i = \rho C_\mu \frac{k^2}{\epsilon} \tag{12}$$

$$C_\mu = \frac{1}{A_0 + A_S U^* k / \epsilon} \tag{13}$$

$$A_0 = 4.0 \tag{14}$$

$$A_S = \sqrt{6} \cos \phi \tag{15}$$

$$\phi = \frac{1}{3} \cos^{-1} (\sqrt{6} W) \tag{16}$$

$$W = \frac{E_{ij} E_{jk} E_{kj}}{(E_{ij} E_{ij})^{1/2}} \tag{17}$$

$$E_{ij} = \frac{1}{2} \left( \frac{\partial u_i}{\partial x_j} + \frac{\partial u_j}{\partial x_i} \right) \quad (18)$$

$$U^* = \sqrt{E_{ij}E_{ij} + \tilde{\Omega}_{ij}\tilde{\Omega}_{ij}} \quad (19)$$

Time average rotation rate tensor:

$$\tilde{\Omega}_{ij} = \Omega_{ij} - 2\varepsilon_{ijk}\omega_k \quad (20)$$

$$\Omega_{ij} = \tilde{\Omega}_{ij} - \varepsilon_{ijk}\omega_k \quad (21)$$

In order to obtain the parameters required for acoustic solution, the jet flow field LES needs to be solved, and the control equations are as follows.

$$\begin{aligned} \frac{\partial}{\partial t}(\rho\bar{u}_i) + \frac{\partial}{\partial x_j}(\rho\bar{u}_i\bar{u}_j) &= -\frac{\partial \bar{p}}{\partial x_i} + \frac{\partial}{\partial x_j} \left( \frac{\partial \bar{u}_i}{\partial x_j} \right) - \frac{\partial \tau_{ij}}{\partial x_j} \\ \frac{\partial \rho}{\partial t} + \frac{\partial}{\partial x_j}(\rho\bar{u}_j) &= 0 \end{aligned} \quad (22)$$

The above formula is the equation in the instantaneous state, and the quantity with the overline in the formula is the filtered field variable. The scale effect of the compressed lattice  $\tau_{ij}$  is

$$\tau_{ij} = \rho\bar{u}_i\bar{u}_j - \rho\bar{u}_i\bar{u}_j \quad (23)$$

The compressible flow field is analyzed according to the above formula, and the uniform-diameter nozzle and the standard nozzle model are used for adaptive grid division. Given a compressed air pressure of 212,782 Pa and a compressed air temperature of 303 K, the following visualization cloud diagram of turbulent velocity is obtained.

In Figure 4 is the velocity cloud map of the equal-diameter nozzle. There is a two-way triangular high-speed area at the nozzle outlet, with a flow rate of 408 M/s. After that, it presents a free jet shape and continues to affect  $L_{CV2}$ .

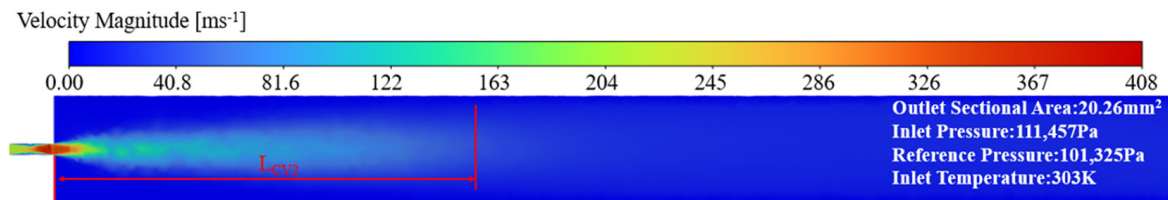


**Figure 4.** Turbulence velocity cloud map of the equal-diameter nozzle with a compressed air pressure of 212,782 Pa and a temperature of 303 K.

In Figure 5 is the standard nozzle velocity cloud map. There is a one-way triangular high-speed area at the nozzle outlet, with a flow velocity of 357 m/s, and then it presents a free jet shape and continues to affect the  $L_{BV2}$ . The following pictures are produced by enlarging the jet outlet area of the two nozzles.

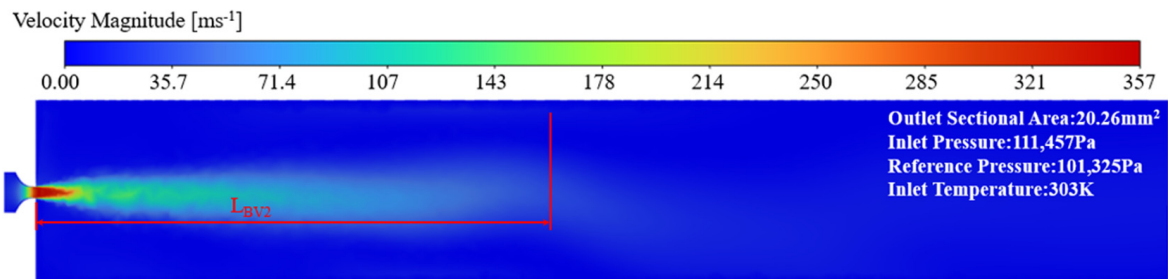


**Figure 5.** Turbulence velocity cloud diagram of the standard Nozzle with a compressed air pressure of 212,782 Pa and a temperature of 303 K.

In Figure 6 is a detailed view of the jet outlet of the equal-diameter nozzle and the standard nozzle. The jet core area and the jet mixing area are divided to obtain the included angle and length of the jet core area and the included angle of the jet mixing area. The specific values are shown in the table below.

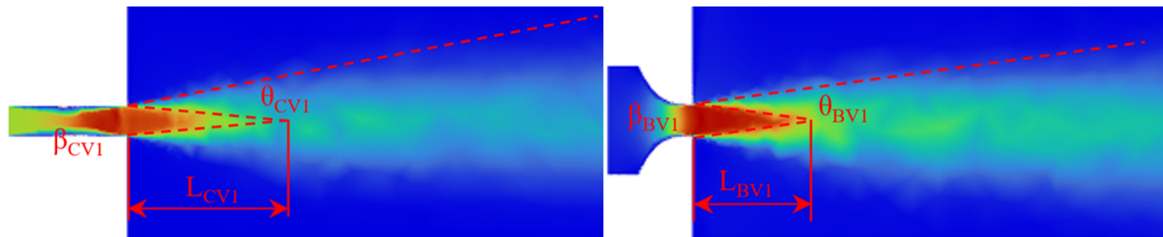


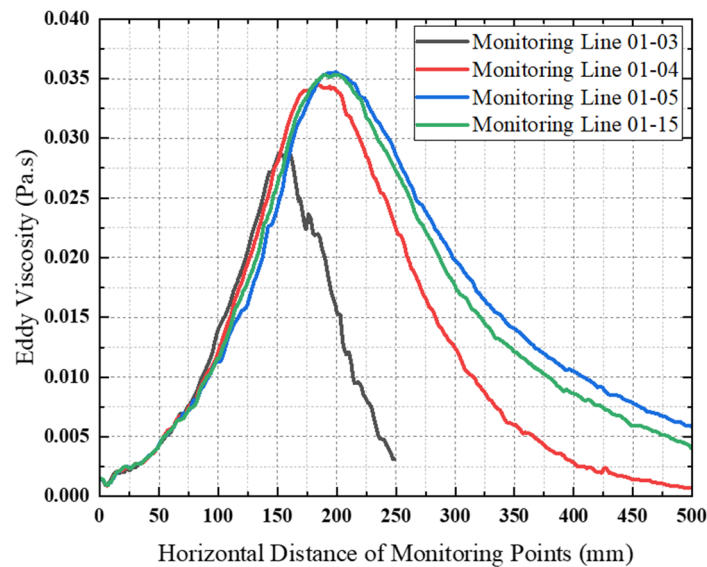
**Figure 6.** Detailed cloud map of the jet outlets of the equal-diameter nozzle and the standard nozzle with a compressed air pressure of 212,782 Pa and a temperature of 303 K.

In Table 1, it can be seen intuitively that under the same compressed air pressure and compressed air temperature, meaning only the nozzle types are different, the angle of the turbulent mixing layer of the equal-diameter nozzle is  $\theta_{CV1} 15.81^\circ$ , while the angle of the turbulent mixing layer of the standard nozzle is  $\theta_{CV1} 15.81^\circ$ . The included angle is  $\theta_{BV1} 15.46^\circ$ , which is basically the same. The included angle of the turbulent core layer of the equal-diameter nozzle is  $\beta_{CV1} 15.21^\circ$ , and the included angle of the turbulent core layer of the equal-diameter nozzle is  $\beta_{BV1} 17.19^\circ$ , which is 68.36% higher than that of the equal-diameter nozzle. Finally, the effective turbulent length  $L_{CV2}$  of the equal-diameter nozzle is 188.56 mm, and the effective turbulent length  $L_{BV2}$  of the standard nozzle is 227.10 mm, which represents an increase of 20.44% compared with the equal-diameter nozzle. The turbulent cloud map is intuitive but not concrete. In order to understand more turbulent details, the specific trend analysis of the two nozzle flow fields is carried out in accordance with the detection line in Figure 2.

**Table 1.** Parameters of the jet outlet of the equal-diameter nozzle and the standard nozzle with a compressed air pressure of 212,782 Pa and a temperature of 303 K.

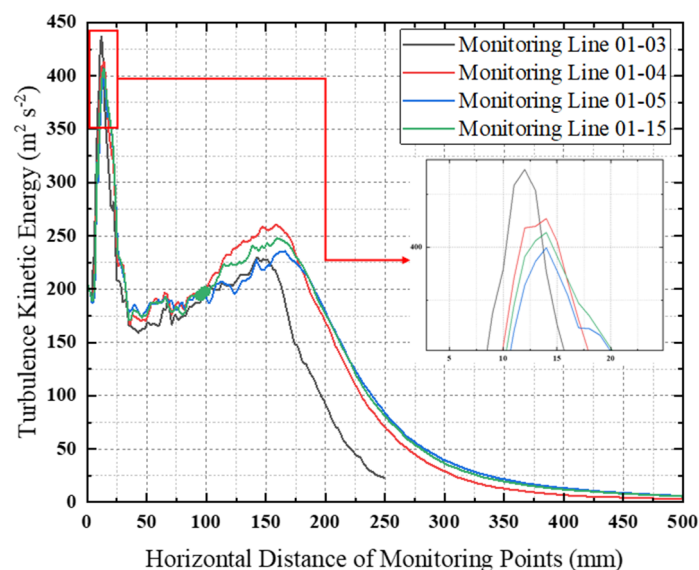
Nozzle Type	$L_{CV2}/L_{BV2}$	$L_{CV1}/L_{BV1}$	$\theta_{CV1}/\theta_{BV1}$	$\beta_{CV1}/\beta_{BV1}$
Equal-Diameter	188.56	13.68	15.81	15.21
Standard	227.10	14.99	15.46	17.19

Figure 7 presents a broken line chart of the eddy viscosity detection line with a pressure of 212,782 Pa and a temperature of 303 K in the flow field of the equal-diameter nozzle. It can be seen from the figure that the four detection lines all show a trend of rising first and then falling, but the turning points are different. When the angle of the jet axis is  $5.484^\circ$ , the detection line turns at 150 mm away from the jet outlet, and the maximum value is 0.0386 Pa.s. When the included angle of the jet axis is  $2.748^\circ$ , the detection line turns at 180 mm away from the jet outlet and the maximum value is 0.039 Pa.s., The detection line with a jet axis angle of  $1.375^\circ$  and the jet axis turn at 200 mm away from the jet outlet, and the maximum value is 0.0307 Pa.s. In the upward trend, the four detection lines climb almost in parallel, and the value changes little, but there is a big difference in the value after the turning point, following the principle that the larger the deflection angle of the jet axis, the sooner the line turns and falls.



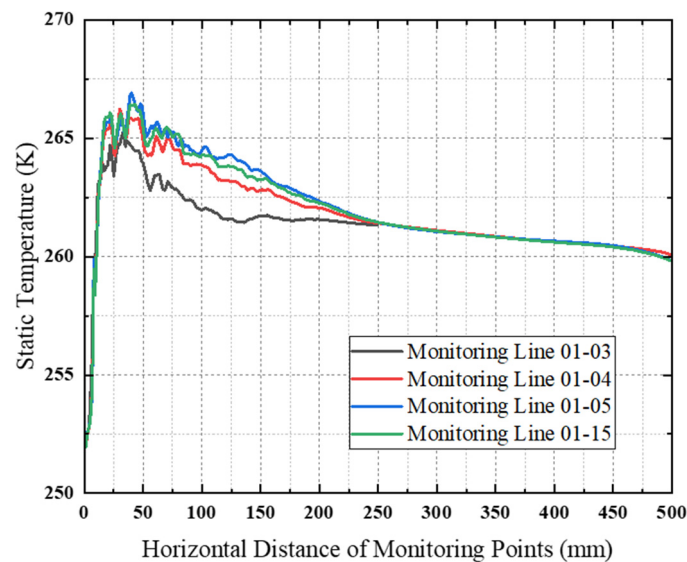
**Figure 7.** Line chart of the eddy viscosity of the equal-diameter nozzle flow field with a compressed air pressure of 212,782 Pa and a temperature of 303 K.

Figure 8 presents a line chart of the turbulent kinetic energy in the flow field of the equal-diameter nozzle with a compressed air pressure of 212,782 Pa and a temperature of 303 K. In the flow field within 500 mm of the jet outlet, the turbulent kinetic energy displays three concentrated transitions. The first transition occurs 12 mm away from the jet outlet. Due to the graph being too compact, we perform local amplification of this section of the detection line. The detection line with a jet axis angle of  $5.484^\circ$  has its first turning point at 24 mm away from the jet outlet, and the maximum value is  $455 \text{ m}^2 \text{ s}^{-2}$ , while the detection line with a jet axis angle of  $2.748^\circ$  also turns at a distance of 24 mm away from the jet outlet. The first inflection occurs at 14 mm, and the maximum value is  $432 \text{ m}^2 \text{ s}^{-2}$ . The detection line with a jet axis angle of  $1.375^\circ$  has its first inflection at 14 mm away from the jet outlet, and the maximum value is  $429 \text{ m}^2 \text{ s}^{-2}$ . The jet axis lies at a distance from the jet outlet. The major turning point appears at 14 mm, and the maximum value is  $426 \text{ m}^2 \text{ s}^{-2}$ . The four detection lines have the same turning trend in the second and third transitions affected by turbulence, but the stability is insufficient.



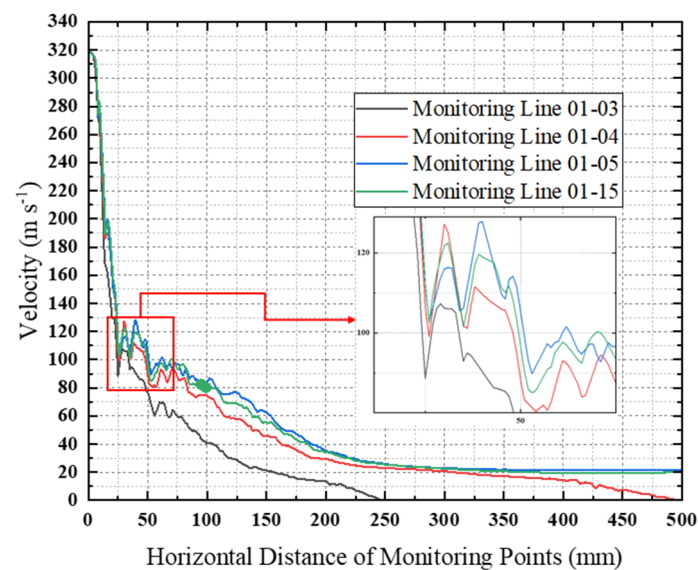
**Figure 8.** Line graph of the turbulent kinetic energy of the equal-diameter nozzle flow field with a compressed air pressure of 212,782 Pa and a temperature of 303 K.

Figure 9 presents a line chart of the flow field of the equal-diameter nozzle with a compressed air pressure of 212,782 Pa in the and a static temperature of 303 K. Four detection lines overlap and rise within 10 mm from the jet outlet, and then show a staggered and unstable trend, overlapping at 250 mm away from the jet outlet, after which they decline. The static temperature of the detection line with the included angle of the jet axis of  $5.484^\circ$  is consistently the lowest, and the static temperature of the jet axis is the highest, but the maximum values of the static temperature of the four detection lines are all below  $0^\circ\text{C}$ .



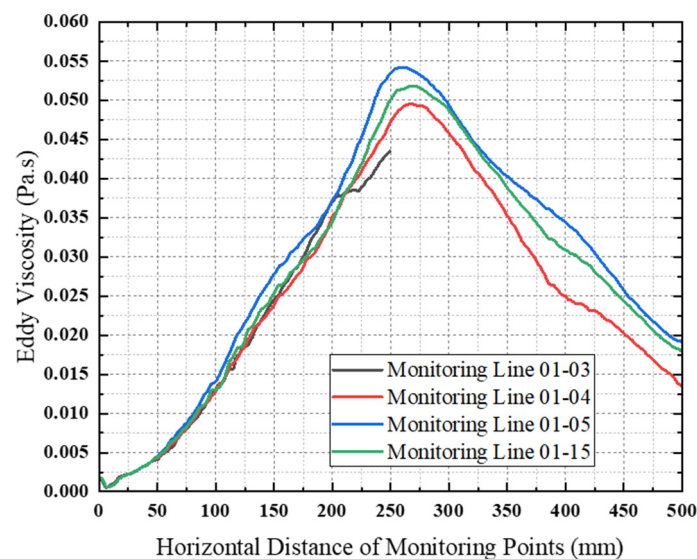
**Figure 9.** Line chart of the static temperature of the equal-diameter nozzle flow field. The compressed air pressure is 212,782 Pa. The temperature is 303 K.

Figure 10 presents a broken line chart of the turbulent velocity for the flow field of the equal-diameter nozzle with a compressed air pressure of 212,782 Pa and a temperature of 303 K. The four detection lines all show that the velocity drops sharply within 25 mm away from the jet outlet, and two lines appear between 25 mm and 50 mm away from the jet outlet. A short-term upward trend is observed, and then the line gradually oscillates and declines. This is regarded as the boundary between the turbulent core area and the turbulent mixed layer, and the airflow is unstable.



**Figure 10.** Line graph of the turbulent velocity of the equal-diameter nozzle flow field with a compressed air pressure of 212,782 Pa and a temperature of 303 K.

Figure 11 is a line chart of the eddy viscosity of the standard nozzle flow field with a compressed air pressure of 212,782 Pa and a temperature of 303 K, and it can be seen from the figure that the detection line with a jet axis angle  $5.484^\circ$  always has an upward trend and the maximum value is 0.0481 Pa.s. The remaining three detection lines all show a trend of rising first and then falling, but the turning points are different. The detection line with an included angle of the jet axis of  $2.748^\circ$  turns at 263 mm away from the jet outlet, and the maximum value was 0.0539 Pa.s. The detection line with an included angle of the jet axis of  $1.375^\circ$  turns at 265 mm away from the jet outlet, and the maximum value is 0.0559 Pa.s. In the upward trend, the four detection lines climb almost in parallel, and the value changes little, but after the turning point, the value of the three detection lines shows a small difference, following the principle that the larger the deflection angle of the jet axis, the earlier the turning point.



**Figure 11.** Line chart of the eddy viscosity of the standard nozzle flow field with a compressed air pressure of 212,782 Pa and a temperature of 303 K.

Figure 12 presents a line chart of the turbulent kinetic energy of the standard nozzle flow field with a pressure of 212,782 Pa and a temperature of 303 K. In the flow field up to 500 mm away from the jet outlet, the turbulent kinetic energy displays three collective transitions. The first transition occurs 20 mm after the jet outlet. Because the graph is too compact, we perform local amplification in the figure. The detection line with a jet axis angle of  $5.484^\circ$  has its first turning point at 18 mm from the jet outlet, and the maximum value is  $349 \text{ m}^2 \text{ s}^{-2}$ , and the detection line with a jet axis angle of  $2.748^\circ$  turn at 9 mm away from the jet outlet. The first inflection is present at  $337 \text{ m}^2 \text{ s}^{-2}$ , and the maximum value is  $337 \text{ m}^2 \text{ s}^{-2}$ . When the jet axis angle is  $1.375^\circ$ . The detection line has a singular inflection at 9 mm away from the jet outlet, and the maximum value is  $325 \text{ m}^2 \text{ s}^{-2}$ . The jet axis is 9 mm away from the jet outlet. The major turning point occurs at  $325 \text{ m}^2 \text{ s}^{-2}$ , and the maximum value is  $325 \text{ m}^2 \text{ s}^{-2}$ . In the second and third transitions, the four detection lines are hit by turbulence in the same turning trend, but the stability is insufficient.

Figure 13 presents a line chart of the standard nozzle flow field with a compressed air pressure of 212,782 Pa and a static temperature of 303 K. The four detection lines overlap and rise within 10 mm away from the jet outlet, and then show a staggered and unstable trend, overlapping and decreasing until 250 mm away from the jet outlet, and then rising again. The static temperature of the detection line with an included angle of the jet axis of  $5.484^\circ$  is always the lowest, and the static temperature of the jet axis is the highest, but the maximum values of the static temperature of the four detection lines are all near  $0^\circ \text{C}$ .

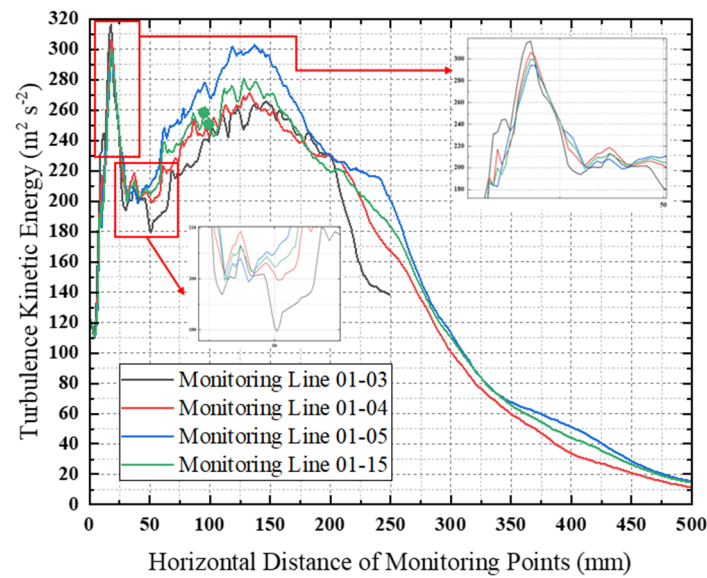


Figure 12. Turbulent kinetic energy of the standard nozzle flow field with a compressed air pressure of 212,782 Pa and a temperature of 303 K.

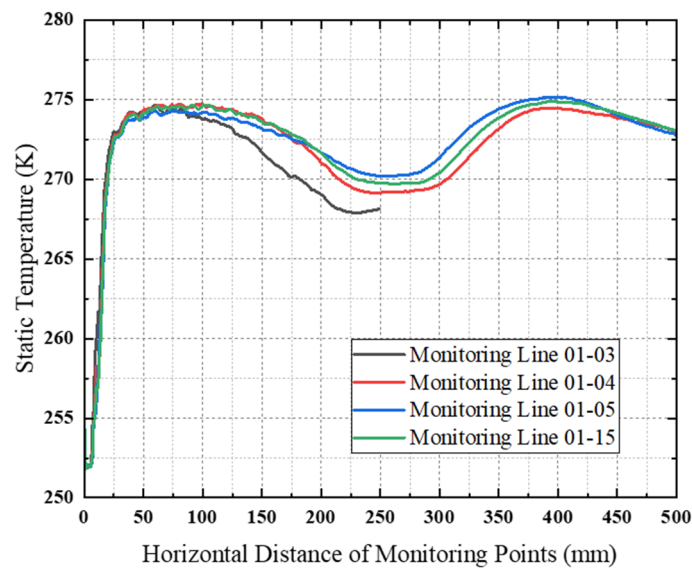


Figure 13. Standard nozzle flow field compressed air pressure 212,782 Pa, temperature 303 K static temperature detection line chart.

Figure 14 presents a line chart of the turbulent velocity of the standard nozzle flow field with a compressed air pressure of 212,782 Pa and a temperature of 303 K. The four detection lines all show that the velocity drops sharply within 25 mm away from the jet outlet, and a short period occurs between 25 mm and 50 mm away from the jet outlet. The detection lines present an upward trend, and then gradually oscillate and declines. This is regarded as the boundary between the turbulent core area and the turbulent mixed layer, and the airflow is unstable.

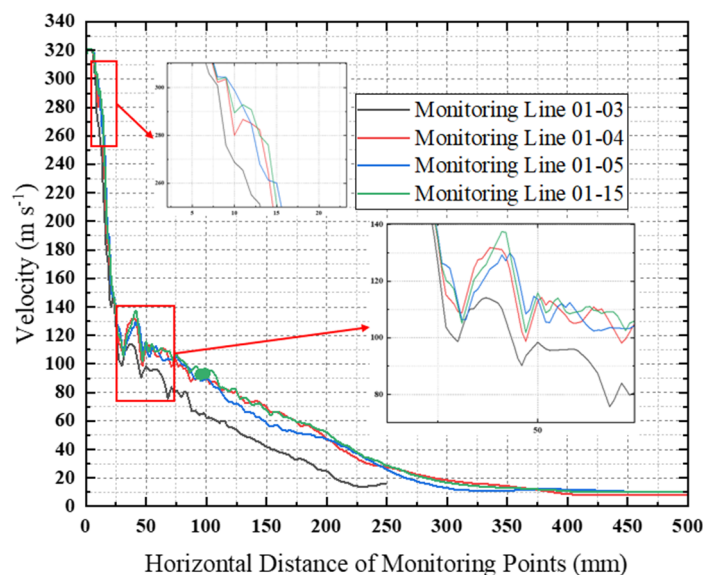


Figure 14. Line chart of the turbulent velocity of the standard nozzle flow field with a compressed air pressure of 212,782 Pa and a temperature of 303 K. Study on Correlation of Jet Noise.

#### 4. Study on Correlation of Jet Noise

As a branch of aeroacoustics, the classical equation of the calculation of jet noise is the Lighthill equation [31]:

$$\frac{\partial^2 \rho'}{\partial t^2} - c_0^2 \frac{\partial^2 \rho'}{\partial x_j^2} = \frac{\partial^2 T_{ij}}{\partial x_i \partial x_j} \tag{24}$$

Lighthill tensor:

$$T_{ij} = \rho v_i v_j + (p' - c_0^2 \rho') \delta_{ij} - \sigma_{ij} \tag{25}$$

For high Reynolds numbers,  $(p' - c_0^2 \rho') \delta_{ij} = 0$ , and an isentropic condition  $\sigma_{ij} = 0$ , Green’s function  $G_0 = (t, x | \tau, y) = \frac{\delta(t - \tau - |x - y|)}{4\pi c_0^2 |x - y|}$  is introduced to solve it.

$$4\pi c_0^2 \rho'(x, t) = \frac{\partial^2}{\partial x_i \partial x_j} \iiint_v \left[ \frac{T_{ij}}{|x - y|} \right] d^3 y \tag{26}$$

The right side of the equation is the quadrupole. Since the nozzle is a high-speed free jet in this paper, only the influence of the quadrupole sound source is considered.

##### 4.1. Near Field Characteristics

We perform the calculation of the free jet noise of the equal-diameter nozzle and the standard nozzle, considering the influence of the quadrupole, according to the monitoring points of the near-field noise field in the figure.

Figure 15 displays the 100 Hz near-field sound pressure level nephogram of the equal-diameter nozzle. The maximum noise at the free jet outlet is 194 dB, and the noise gradually weakens with the increase in the jet distance. The overall trend is in line with the free jet velocity field nephogram.

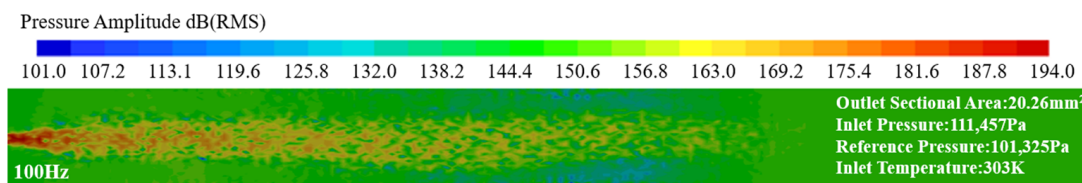


Figure 15. Cloud map of the 100 Hz near-field sound pressure levels of the equal-diameter nozzle.

Figure 16 shows the 1000 Hz near-field sound pressure level nephogram of the equal-diameter nozzle. The maximum noise in the free jet noise field reaches 133 dB. With the increase in the jet distance, the noise shows a diffusion trend, and the variation range is small in the entire near-field noise field. High values of jet noise affect the entire near-field noise field.

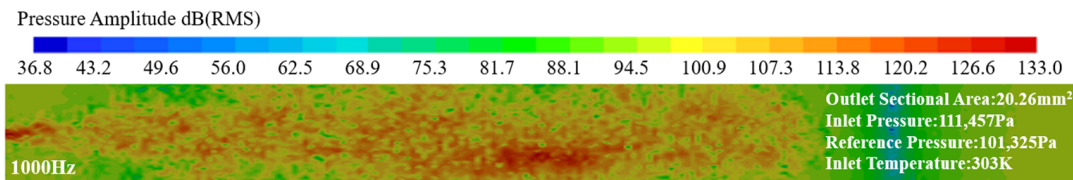


Figure 16. Cloud map of the 1000 Hz near-field sound pressure levels of the equal-diameter nozzle.

Figure 17 displays the nephogram of the near-field sound pressure level of the equal-diameter nozzle at 2000 Hz. The maximum noise in the free jet noise field reaches 123 dB. With the increase in the jet distance, the noise shows a diffusion trend, and the change range is moderate in the entire near-field noise field. The turbulent velocity field is slightly diffused but the trend is consistent.

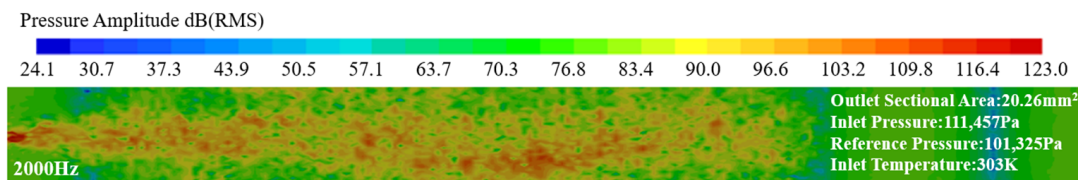


Figure 17. Cloud map of the 2000 Hz near-field sound pressure levels of the equal-diameter nozzle.

Figure 18 presents the nephogram of the near-field sound pressure level of the equal-diameter nozzle at 3000 Hz. The maximum noise in the free jet noise field reaches 114 dB in many places. With the increase in the jet distance, the noise shows a diffusion trend. The turbulent velocity field is slightly diffused but the trend is consistent.

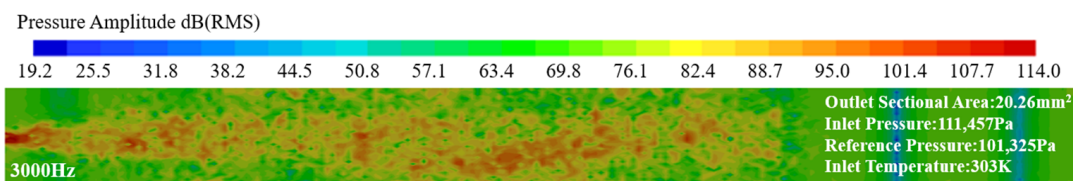


Figure 18. Cloud map of the 3000 Hz near-field sound pressure levels of the equal-diameter nozzle.

Figure 19 is a line graph of the frequency response curve of the 3000 Hz near-field sound pressure level of the equal-diameter nozzle. According to the 3000 Hz near-field monitoring point data obtained in Figure 2, the sound pressure level gradually decreases with the increase in the frequency, and the overall sound pressure level is the maximum value. The minimum value is higher than 50 dB, while the maximum value is 170 dB, and the maximum and minimum values of the near-field monitoring points vary by 40 dB.

Figure 20 displays the 100 Hz near-field sound pressure level nephogram of the standard nozzle. The maximum noise at the free jet outlet is 185 dB, and the noise gradually weakens with the increase in the jet distance. The overall trend is consistent with the free jet velocity field cloud diagram.

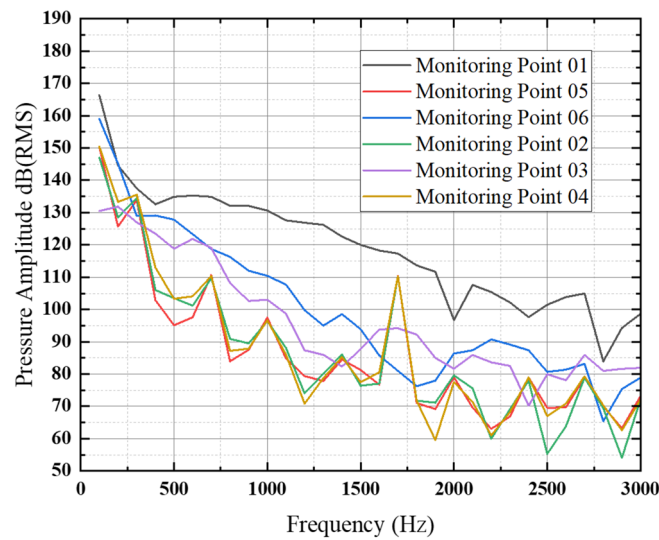


Figure 19. Line graph of the frequency response curve of the equal-diameter nozzle with a 3000 Hz near-field sound pressure level.

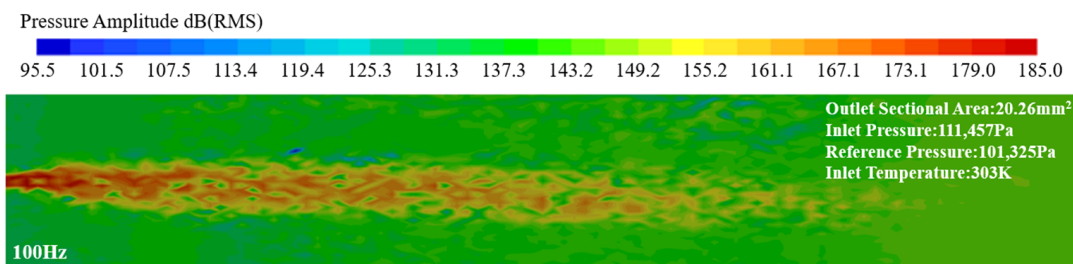


Figure 20. Cloud map of the 100 Hz near-field sound pressure levels of the standard nozzle.

Figure 21 shows the 1000 Hz near-field sound pressure level nephogram of the standard nozzle. The maximum noise in the free jet noise field reaches 131 dB. With the increase in the jet distance, the noise shows a diffusion trend, and the noise influence is concentrated in the tail of the near-field detection field.

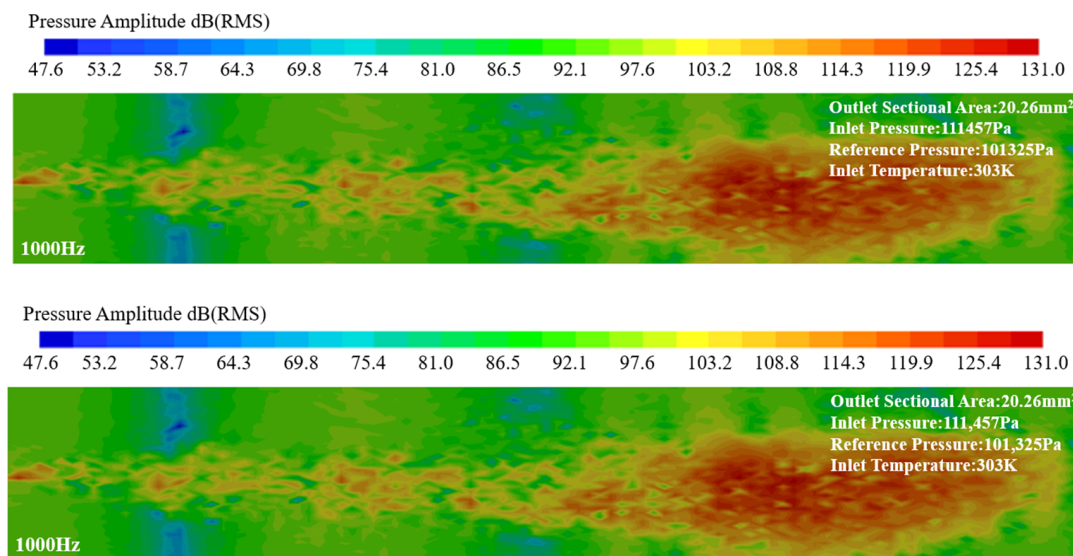
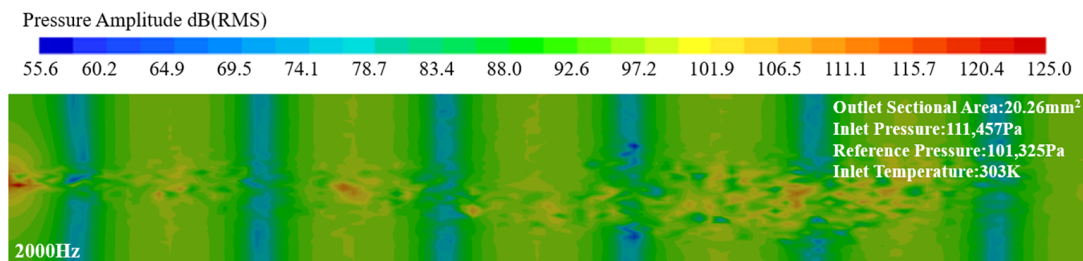


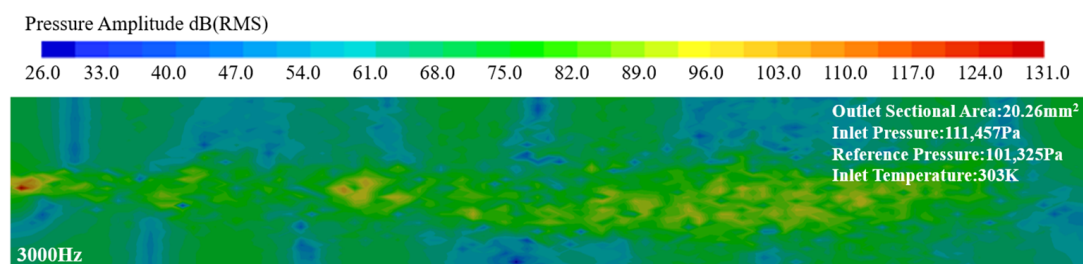
Figure 21. Cloud map of the 1000 Hz near-field sound pressure levels of the standard nozzle.

Figure 22 displays the nephogram of the near-field sound pressure level of the standard nozzle at 2000 Hz. The maximum noise in the free jet noise field reaches 125 dB in many places, but there is an interference effect. The entire near-field noise field displays six equidistant low vocal bands. A small area of concentrated noise appears.



**Figure 22.** Cloud map of the 2000 Hz near-field sound pressure levels of the standard nozzle.

Figure 23 shows the 3000 Hz near-field sound pressure level nephogram of the standard. The noise at the exit of the free jet noise field reaches 131 dB. With the increase in the jet distance, the noise shows a diffusion trend, and the change range is moderate in the entire near-field noise field, and there is a symmetrical noise interference phenomenon.



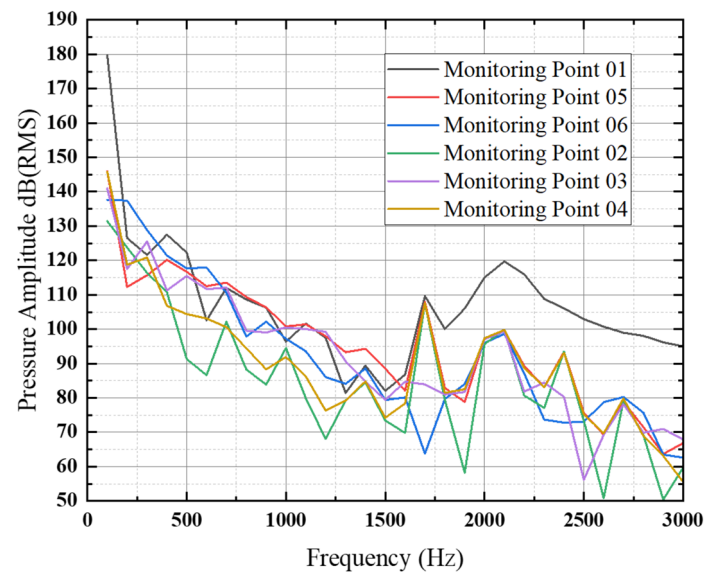
**Figure 23.** Cloud map of the 3000 Hz near-field sound pressure levels of the standard nozzle.

Figure 24 is a line graph of the frequency response curve of the 3000 Hz near-field sound pressure level of the standard nozzle. According to the 3000 Hz near-field monitoring point data obtained in Figure 2, the sound pressure level gradually decreases with the increase in frequency, and the maximum overall sound pressure level is close to 180 dB, while the minimum value of is higher than 50 dB, and the maximum and minimum changes in the near-field monitoring points are within 50 dB.

#### 4.2. Far Field Characteristics

Through the calculation of free jet noise for equal-diameter nozzles and standard nozzles considering the influence of quadrupoles, the sound pressure level nephograms under four frequency responses are mainly analyzed according to the monitoring points of the far-field noise field in Figure 3. The polar coordinate system in the figure draws 300 mm, 600 mm, 900 mm and 1500 mm concentric reference circles with the center of the nozzle outlet as the origin, and divides the reference angles to facilitate analysis.

Figure 25 presents the 100 Hz and 1000 Hz far-field sound pressure level nephograms of the equal-diameter nozzle. In the 100 Hz sound pressure level nephogram, the noise radiates to the jet in the forward and reverse directions in a circular arc, with the far end of the jet fluid domain as the dividing line. In the 1000 Hz sound pressure level nephogram, the noise radiates symmetrically in the forward and reverse directions of the jet, with the middle end of the jet fluid domain as the dividing line, and the radiation in the direction of the jet axis is weak and the noise is radiated in a cone with a cone angle of 65 from the nozzle outlet to the jet direction.



**Figure 24.** Line graph of the frequency response curve of the 3000 Hz near-field sound pressure level of the standard nozzle.

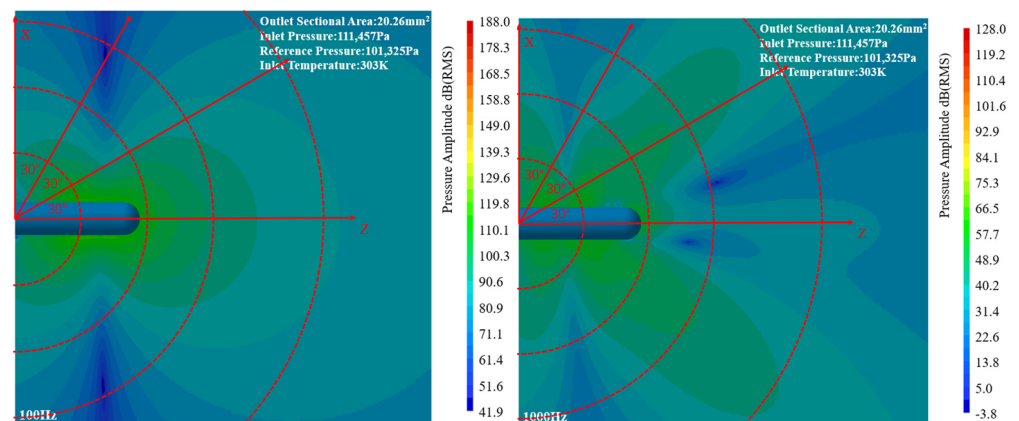


**Figure 25.** Nephograms of the 100 Hz and 1000 Hz far-field sound pressure levels of equal-diameter nozzles.

Figure 26 presents the 2000 Hz and 3000 Hz far-field sound pressure level nephograms of the equal-diameter nozzle. In the 2000 Hz sound pressure level nephogram, the noise radiates in a corrugated shape from the jet outlet to the jet direction. In the 3000 Hz sound pressure level nephogram, the noise is the jet flow. The outlet as the starting point radiates in a zigzag shape to the jet direction and adjacent serrations at an angle of  $15^\circ$ .

Figure 27 presents the 100 Hz and 1000 Hz far-field sound pressure level nephograms of the standard nozzle. In the 100 Hz sound pressure level nephogram, the noise is radiated in a circular arc in the forward and reverse directions of the jet, with the middle end of the jet fluid domain as the dividing line. At 1000 Hz, in the sound pressure level cloud map, the noise radiates irregularly to the surroundings with the jet fluid domain as the reference, and there is a clear dividing line at the middle end of the jet fluid domain. The noise radiates in an asymmetric cone shape from the nozzle outlet in the jet direction.

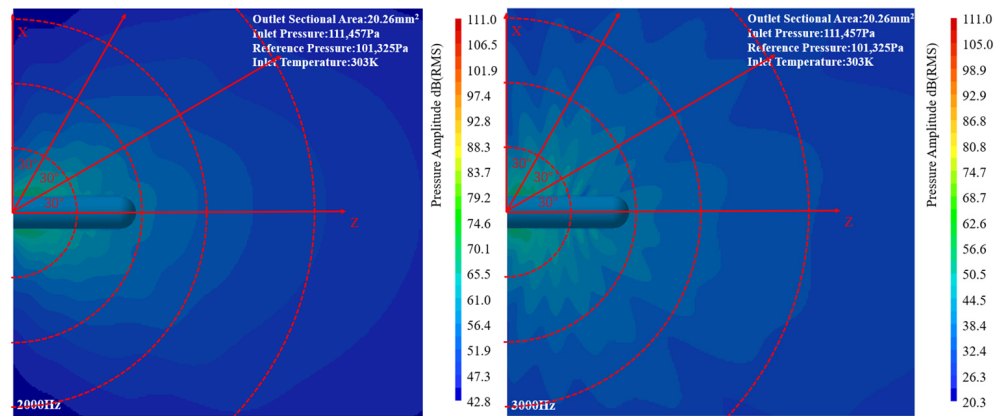


Figure 26. Nephograms of the 2000 Hz and 3000 Hz far-field sound pressure levels of equal-diameter nozzles.

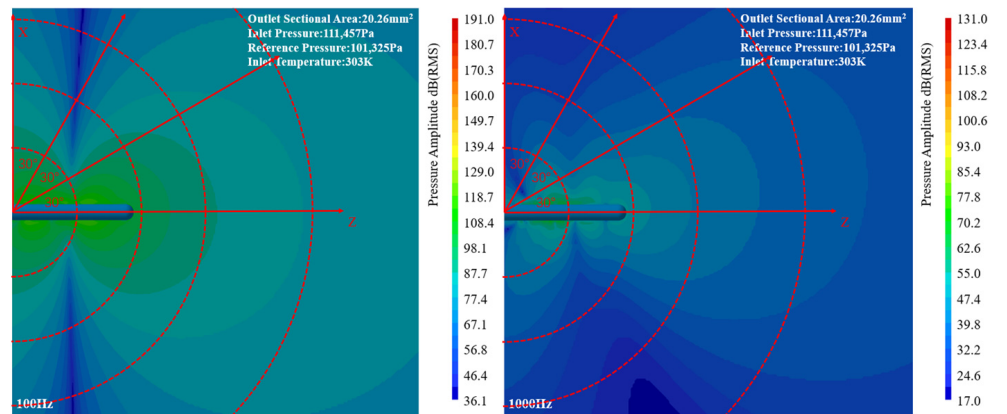


Figure 27. Nephograms of the 100 Hz and 1000 Hz far-field sound pressure levels of standard nozzles.

Figure 28 displays the 2000 Hz and 3000 Hz far-field sound pressure level nephograms of the standard nozzle. In the 2000 Hz sound pressure level nephogram, the noise picks up the jet outlet as the jet fluid domain and radiates irregularly in a corrugated shape. In the 3000 Hz sound pressure level nephogram, the noise, starting from the jet outlet, radiates in a zigzag shape in the jet direction, and the noise is radiated in an asymmetric conical shape with a cone angle of 60° from the nozzle outlet in the jet direction.

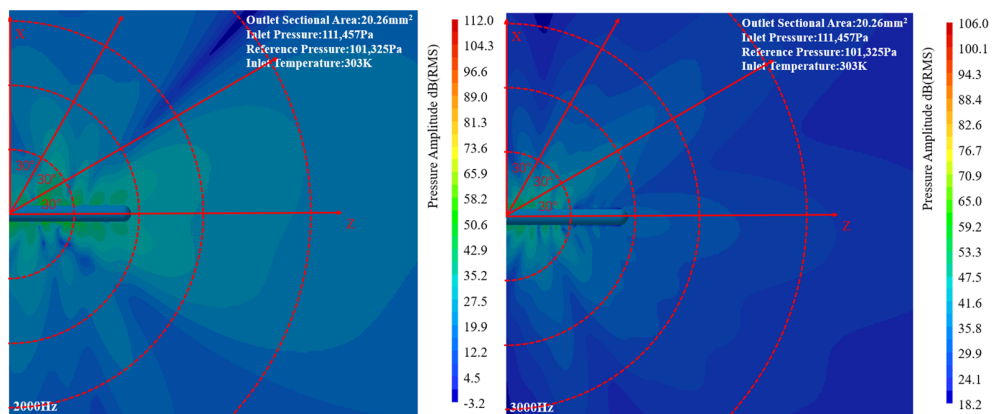
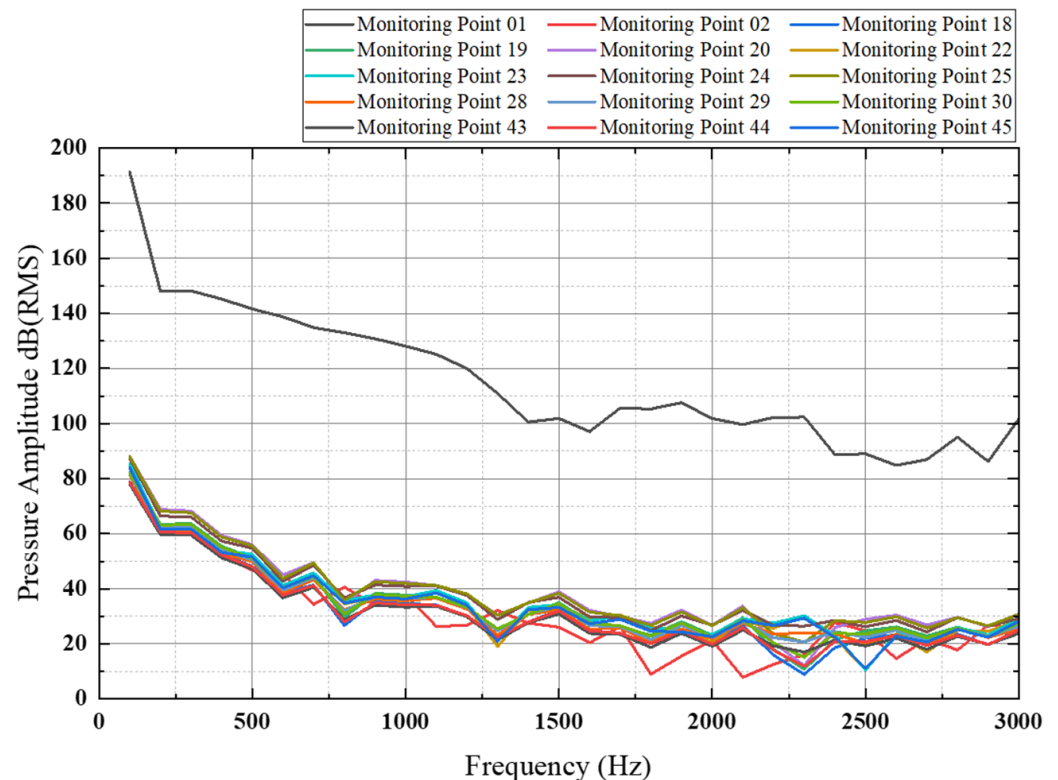


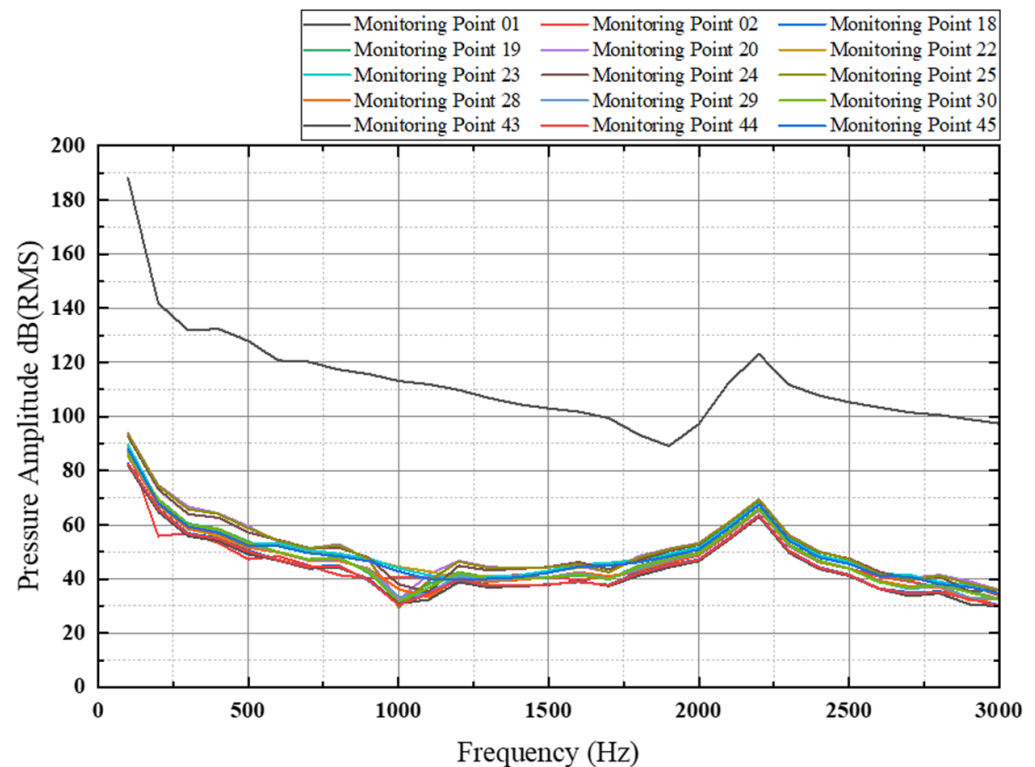
Figure 28. Nephograms of the 2000 Hz and 3000 Hz far-field sound pressure levels of standard nozzles.

Figure 29 is a line graph of the frequency response curve of the 3000 Hz far-field sound pressure level of the equal-diameter nozzle. According to the 3000 Hz near-field monitoring point data obtained in Figure 3, the sound pressure level gradually declines with the increase in the frequency, and the overall sound pressure level is the maximum value, which is close to 190 dB. The minimum value is higher than 10 dB, and the maximum and minimum changes in the far-field monitoring points are within 190 dB. From the line graph, it can be found that the sound pressure level of the jet outlet is much higher than the sound pressure level of the other far-field monitoring points and has a different trend. A downward tendency and similar sound pressure levels are observed.



**Figure 29.** Line graph of the frequency response curve of the 3000 Hz far-field sound pressure level of the equal-diameter nozzle.

Figure 30 is a line graph of the frequency response curve of the 3000 Hz near-field sound pressure level of the standard nozzle. According to the 3000 Hz far-field monitoring point data obtained in Figure 3, the sound pressure level gradually decreases as the frequency increases, and the overall maximum sound pressure level is close to 190 dB, while the minimum value is higher than 30 dB, and the maximum and minimum changes in the near-field monitoring point are within 160 dB. From the line graph, it can be clearly found that the sound pressure level of the jet outlet is much higher than the sound pressure level of other far-field monitoring points, and the change trend is the same. A downward trend and similar sound pressure levels are observed.



**Figure 30.** Line graph of the frequency response curve of the 3000 Hz far-field sound pressure level of the standard nozzle.

## 5. Conclusions

The equal-diameter nozzles and standard nozzles are designed with equal outlet cross-sectional areas and 3D printed. According to the characteristics of free jets, a concentric dichotomy method is proposed to arrange monitoring points, and the fluid analysis is carried out with the help of the free-flowing Realizable  $k - \epsilon$  model of fluid analysis jets. We substitute the fluid analysis results into the Lighthill equation excited by the quadrupole sound source to solve the noise field, and compare the single-variable results of the equal-diameter nozzle and the standard nozzle, and the following conclusions are drawn:

- Under the same boundary conditions, the jet angle in the turbulent core area of the equal-diameter nozzle flow field is  $0.35^\circ$  larger than that of the standard nozzle under the free flow field of the two nozzle jets, and the angle of the turbulent mixing area is  $1.98^\circ$  larger than that of the standard nozzle. The trend remains the same.
- In the case of the same boundary conditions, the near-field noise reduction law of the medium diameter nozzle is better than that of the standard nozzle in the jet noise field of the two nozzles, and the propagation law of low-frequency noise in the near-field noise field is better than that of high-frequency noise, and the interference is less attenuated. The directivity of high-frequency noise in the far-field noise field is more pronounced and decays slower than lower-frequency noise.
- The line graph of the sound pressure level shows that in the two TPS nozzles, the sound pressure level mainly occurs at the nozzle outlet.

By analyzing the flow field and the sound field of equal-diameter nozzles and standard nozzles, we can truly understand some of the noise characteristics of standard nozzles, and the flow field and sound field characteristics of the two scaled nozzles of TPS can provide an optimal direction for the parameter design of TPS nozzles and improve the accuracy of the flow and pressure ratio of the TPS-simulated aero-engine.

**Author Contributions:** G.M. and Q.L. contributed to the main idea of this paper; G.M. and Y.L. performed the experiments, analyzed the data and wrote the paper. All authors have read and agreed to the published version of the manuscript.

**Funding:** This research was financially supported by Harbin Aerodynamics Research Institute's TPS and its measurement and control system, lubrication system and standard nozzle procurement project (Grant No. 2020-HY-001-JG-F) and Jilin Province Science and Technology Development Plan Project (Grant No. 192487GX010367334). This research was financially supported by the Jilin Province Innovation Center of Aerodynamic Science and Technology.

**Institutional Review Board Statement:** Not applicable.

**Informed Consent Statement:** Not applicable.

**Data Availability Statement:** Not applicable.

**Conflicts of Interest:** The authors declare no conflict of interest.

## References

1. Zarastvand, M.R.; Asadijafari, M.H.; Talebitooti, R. Improvement of the Low-Frequency Sound Insulation of the Poroelastic Aerospace Constructions Considering Pasternak Elastic Foundation. *Aerosp. Sci. Technol.* **2021**, *112*, 106620. [[CrossRef](#)]
2. Rahmatnezhad, K.; Zarastvand, M.R.; Talebitooti, R. Mechanism Study and Power Transmission Feature of Acoustically Stimulated and Thermally Loaded Composite Shell Structures with Double Curvature. *Compos. Struct.* **2021**, *276*, 114557. [[CrossRef](#)]
3. Zarastvand, M.; Ghassabi, M.; Talebitooti, R. Prediction of Acoustic Wave Transmission Features of the Multilayered Plate Constructions: A Review. *J. Sandw. Struct. Mater.* **2022**, *24*, 218–293. [[CrossRef](#)]
4. Huff, D.L. NASA Glenn's Contributions to Aircraft Engine Noise Research. *J. Aerosp. Eng.* **2013**, *26*, 218–250. [[CrossRef](#)]
5. Fields, J.M. Effect of Personal and Situational Variables on Noise Annoyance in Residential Areas. *J. Acoust. Soc. Am.* **1993**, *93*, 2753–2763. [[CrossRef](#)]
6. Trost, R.P.; Shaw, G.B. Statistical Analysis of Hearing Loss among Navy Personnel. *Mil. Med.* **2007**, *172*, 426–430. [[CrossRef](#)] [[PubMed](#)]
7. Krumme, A.; Hegen, S.; Nahuis, R. Design of a Multi-Stage Axial Turbine within the Scope of Complete System Design, Manufacturing and Operation of a New Turbine Propulsion Simulator (TPS). In Proceedings of the 33rd AIAA Applied Aerodynamics Conference, Dallas, TX, USA, 19 June 2015; American Institute of Aeronautics and Astronautics: Reston, VA, USA, 2015.
8. Lighthill, M.J. On Sound Generated Aerodynamically I. General Theory. *Proc. R. Soc. Lond. Ser. A Math. Phys. Sci.* **1952**, *211*, 564–587. [[CrossRef](#)]
9. Lighthill, M.J. On Sound Generated Aerodynamically II. Turbulence as a Source of Sound. *Proc. R. Soc. Lond. Ser. A Math. Phys. Sci.* **1954**, *222*, 1–32. [[CrossRef](#)]
10. Goldstein, M.E. Aeroacoustics of Turbulent Shear Flows. *Annu. Rev. Fluid Mech.* **1984**, *16*, 263–285. [[CrossRef](#)]
11. McLaughlin, D.K.; Morrison, G.L.; Troutt, T.R. Experiments on the Instability Waves in a Supersonic Jet and Their Acoustic Radiation. *J. Fluid Mech.* **1975**, *69*, 73–95. [[CrossRef](#)]
12. McLaughlin, K. On the Noise Generated by Large Scale Instabilities in Supersonic Jets. In Proceedings of the 6th Aeroacoustics Conference, Hartford, CT, USA, 4–6 June 1980; p. 964.
13. Henderson, B.; Norum, T. Impact of Fluidic Chevrons on Supersonic Jet Noise. In Proceedings of the 13th AIAA/CEAS Aeroacoustics Conference (28th AIAA Aeroacoustics Conference), Rome, Italy, 21–23 May 2007; American Institute of Aeronautics and Astronautics: Reston, VA, USA, 2007.
14. Heeb, N.; Munday, D.; Gutmark, E.; Liu, J.; Kailasanath, K. Supersonic Jet Noise Reduction by Chevrons Enhanced with Fluidic Injection. In Proceedings of the 40th Fluid Dynamics Conference and Exhibit, Chicago, IL, USA, 28 June 2010; American Institute of Aeronautics and Astronautics: Reston, VA, USA, 2010.
15. Mora, P.A.; Kastner, J.F.; Gutmark, E.J.; Kailasanath, K. Investigation of a Heated Supersonic Jet Chevrons Nozzle. In Proceedings of the 53rd AIAA Aerospace Sciences Meeting, Kissimmee, FL, USA, 5 January 2015; American Institute of Aeronautics and Astronautics: Reston, VA, USA, 2015.
16. Dosanjh, D. Some Recent Developments in Supersonic Jet Noise Reduction. In Proceedings of the 2nd Aeroacoustics Conference, Hampton, VA, USA, 24 March 1975; American Institute of Aeronautics and Astronautics: Reston, VA, USA, 1975.
17. Dahl, M.D.; Papamoschou, D. Analytical Predictions and Measurements of the Noise Radiated from Supersonic Coaxial Jets. *AIAA J.* **2000**, *38*, 584–591. [[CrossRef](#)]
18. Debiasi, M.; Papamoschou, D. Noise from Imperfectly Expanded Supersonic Coaxial Jets. *AIAA J.* **2001**, *39*, 388–395. [[CrossRef](#)]
19. Liu, J.; Kailasanath, K.; Ramamurti, R.; Munday, D.; Gutmark, E.; Lohner, R. Large-Eddy Simulations of a Supersonic Jet and Its Near-Field Acoustic Properties. *AIAA J.* **2009**, *47*, 1849–1865. [[CrossRef](#)]

20. Liu, J.; Corrigan, A.T.; Kailasanath, K.; Heeb, N.S.; Munday, D.E.; Gutmark, E.J. Computational Study of Shock-Associated Noise Characteristics Using LES. In Proceedings of the 19th AIAA/CEAS Aeroacoustics Conference, Berlin, Germany, 27 May 2013; American Institute of Aeronautics and Astronautics: Reston, VA, USA, 2013.
21. Liu, J.; Corrigan, A.T.; Kailasanath, K.; Heeb, N.S.; Gutmark, E.J. Numerical Study of Noise Sources Characteristics in An Underexpanded Jet Flow. In Proceedings of the 20th AIAA/CEAS Aeroacoustics Conference, Atlanta, GA, USA, 16 June 2014; American Institute of Aeronautics and Astronautics: Reston, VA, USA, 2014.
22. Bodony, D.; Lele, S. Jet Noise Prediction of Cold and Hot Subsonic Jets Using Large-Eddy Simulation. In Proceedings of the 10th AIAA/CEAS Aeroacoustics Conference, Manchester, UK, 10 May 2004; American Institute of Aeronautics and Astronautics: Reston, VA, USA, 2004.
23. Massey, S.; Elmiligui, A.; Hunter, C.; Thomas, R.; Pao, P.; Mengle, V. Computational Analysis of a Chevron Nozzle Uniquely Tailored for Propulsion Airframe Aeroacoustics. In Proceedings of the 12th AIAA/CEAS Aeroacoustics Conference (27th AIAA Aeroacoustics Conference), Cambridge, MA, USA, 8 May 2006; American Institute of Aeronautics and Astronautics: Reston, VA, USA, 2006.
24. Brès, G.; Nichols, J.; Lele, S.; Ham, F. Towards Best Practices for Jet Noise Predictions with Unstructured Large Eddy Simulations. In Proceedings of the 42nd AIAA Fluid Dynamics Conference and Exhibit, New Orleans, LA, USA, 25 June 2012; American Institute of Aeronautics and Astronautics: Reston, VA, USA, 2012.
25. Tam, C.K.W. Supersonic Jet Noise. *Annu. Rev. Fluid Mech.* **1995**, *27*, 17–43. [[CrossRef](#)]
26. Bridges, J.; Brown, C. Parametric Testing of Chevrons on Single Flow Hot Jets. In Proceedings of the 10th AIAA/CEAS Aeroacoustics Conference, Manchester, UK, 10 May 2004; American Institute of Aeronautics and Astronautics: Reston, VA, USA, 2004.
27. Jawahar, H.K.; Meloni, S.; Camussi, R. Jet Noise Sources for Chevron Nozzles in Under-Expanded Condition. *Int. J. Aeroacoust.* **2022**, 1475472X221101766. [[CrossRef](#)]
28. Proença, A.R.; Meloni, S. Evaluation of Turbulent Jet Characteristic Scales Using Joint Statistical Moments and an Adaptive Time-Frequency Analysis. *Fluids* **2022**, *7*, 125. [[CrossRef](#)]
29. Tinney, C.E.; Jordan, P. The near Pressure Field of Co-Axial Subsonic Jets. *J. Fluid Mech.* **2008**, *611*, 175–204. [[CrossRef](#)]
30. Arndt, R.E.A.; Long, D.F.; Glauser, M.N. The Proper Orthogonal Decomposition of Pressure Fluctuations Surrounding a Turbulent Jet. *J. Fluid Mech.* **1997**, *340*, 1–33. [[CrossRef](#)]
31. Shapiro, A.H. The Dynamics and Thermodynamics of Compressible Fluid Flow: Vol. 1. Available online: <https://www.mysciencework.com/publication/show/dynamics-thermodynamics-compressible-fluid-flow-vol-1-d305bfd0> (accessed on 11 August 2022).
32. Mu, G.; Lyu, Q. Analysis of Turbulent Boundary Layer Jet Flow Pattern of TPS Standard Nozzle. *J. Phys. Conf. Ser.* **2022**, *2228*, 012039. [[CrossRef](#)]